Chapter 1

Nuclear Size and Charge

"Like the radius of an atom, the radius of a nucleus is not a precisely defined quantity."
K. S. Krane

1.1 Posing the problem: how big is a nucleus?

Nuclei are not hard spheres with sharp edges. The density of nucleons and the nuclear potential are relatively constant over short distances and then drop rapidly toward zero. It is therefore natural to characterise the nuclear shape with two parameters: a **mean radius**, where the density is half its central value, and a **skin thickness**, over which the density falls from near its maximum to near zero. A third parameter is needed later for nuclei that are not spherical [6].

A further subtlety is that the radius one measures depends on the experiment. Electromagnetic probes (electron scattering, muonic X rays, optical and X-ray isotope shifts) determine the distribution of *nuclear charge*, mainly the protons. Hadronic probes (α scattering, pionic atoms) determine the distribution of *nuclear matter*, all nucleons. The two distributions are similar but not identical, especially in heavy nuclei with neutron skins [6, 1].

The nuclear size scale is the femtometre (fermi),

$$1\,\text{fm} = 10^{-15}\,\text{m} = 10^{-13}\,\text{cm}. \tag{1.1}$$

Empirically, charge radii satisfy

$$R \simeq r_0\, A^{1/3}, \qquad r_0 \approx 1.2\text{–}1.25\,\text{fm}, \tag{1.2}$$

from electron scattering. That $A^{1/3}$ law is the geometric face of nearly constant central density: if $A/(\frac{4}{3}\pi R^3)$ is roughly constant, then $R \propto A^{1/3}$.

Definition

The constant r_0 depends on the surface definition. Common conventions give

$$r_0 \approx \begin{cases} 1.2 - -1.25\,\text{fm} & \text{(charge / equivalent hard sphere)}, \\ 1.3 - -1.4\,\text{fm} & \text{(strong interaction / } \alpha \text{ scattering)}. \end{cases}$$

Throughout this chapter, $r_0 \approx 1.2\,\text{fm}$ is used for charge radii unless stated otherwise.

Key idea

Wavelength criterion. Two related conventions must not be mixed. The de Broglie wavelength is $\lambda_{\text{dB}} = h/p = 2\pi\hbar/p$, whereas the reduced wavelength $\bar{\lambda} = \hbar/p$ sets the phase-resolution scale. The invariant criterion is $q\ell/\hbar \gtrsim 1$, where q is the momentum transferred to the nucleus. Requiring the stricter optical-style $\lambda_{\text{dB}} \lesssim 10\,\text{fm}$ gives $p \gtrsim 124\,\text{MeV/c}$. High-energy electron beams (100 MeV–1 GeV) provide exactly that [6].

Before writing a single scattering amplitude, it helps to recall why ordinary light cannot answer the size question.

1.1.1 A classroom analogy: chalk and wavelengths

Imagine a stick of chalk, a few centimetres long (Figure 1.1). With the naked eye (that is, with visible light), one can estimate its diameter without effort. Sound waves of ordinary frequencies cannot do the same job. Both light and sound are waves; the difference is their wavelength relative to the object being examined.

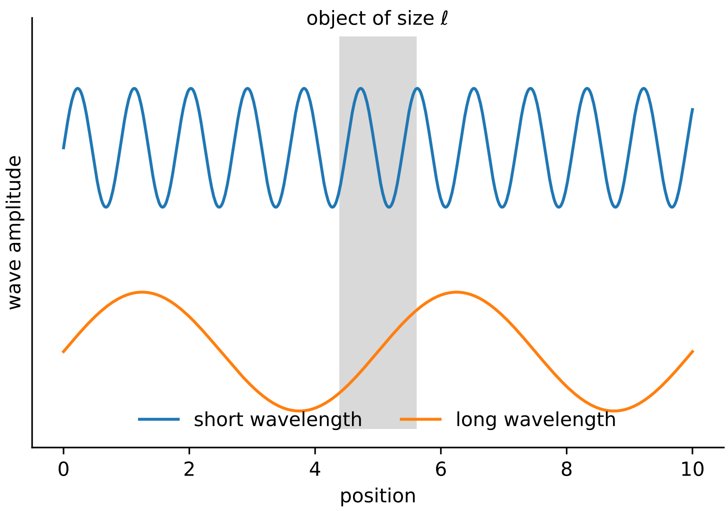

Figure 1.1: Resolution schematic. A short wavelength records structure on the scale ℓ; a much longer wavelength averages over it. Visible light (400–700 nm) has a wavelength far smaller than the diameter of the chalk, so the eye can resolve its size. Audible sound does not.

Visible light spans roughly 400–700 nm, four to seven orders of magnitude smaller than a centimetre-scale object. Audible sound, by contrast, lives in a very different regime. The wavelength of a wave of speed v and frequency ν is

$$\lambda = \frac{v}{\nu}. \tag{1.3}$$

Taking $v \approx 340\,\text{m/s}$ for air and $\nu = 1\,\text{kHz}$ as a representative audible tone, one finds $\lambda \approx 0.34\,\text{m}$—about thirty times larger than the chalk. A wave that long cannot "see" structure on the scale of a centimetre; it simply diffracts around the obstacle as if the obstacle were a point.

Key idea

To resolve a feature of size ℓ, a probe needs wavelength $\lambda \lesssim \ell$. Visible light works for chalk because $\lambda_{\text{light}} \ll \ell_{\text{chalk}}$. Audible sound fails because $\lambda_{\text{sound}} \gg \ell_{\text{chalk}}$. The same criterion decides whether electrons can resolve a nucleus.

The same logic, applied to the nucleus, is unforgiving. Early estimates from α-particle scattering already indicated nuclear radii of order a few fermis (10^{-15}–10^{-14} m). Visible light ($\lambda \sim 10^{-7}$ m) is hopelessly coarse. Even hard γ-rays fall short of the needed resolution. One needs a probe whose de Broglie wavelength is itself of nuclear size (a few fermis or less). High-energy electrons provide precisely that.

Remark

Electrons are preferred over protons or α particles for precision *charge*-density work because the electron–nucleus interaction is electromagnetic and calculable to high accuracy. Strong-interaction probes, while useful for hadronic form factors and neutron distributions, introduce model dependence that electron scattering largely avoids [2, 7]. Mass and charge radii need not agree at the percent level: Coulomb repulsion tends to push protons slightly farther out than neutrons in heavy nuclei.

1.2 Historical path: from Rutherford to Hofstadter

1.2.1 Rutherford scattering and a first radius

Historical note: Ernest Rutherford (1871–1937)

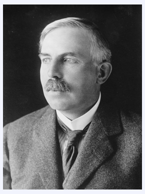

Ernest Rutherford was born in Brightwater, New Zealand, and trained at Canterbury College before moving to the Cavendish Laboratory under J. J. Thomson. After work on radioactivity in Montreal (where he classified α, β, and γ radiation and, with Soddy, formulated radioactive transformation), he took the chair at Manchester in 1907. There, with **Hans Geiger** and **Ernest Marsden**, he directed the α-particle scattering experiments that overthrew the Thomson "plum pudding" atom. In 1911 he proposed that essentially all the atomic mass and positive charge sit in a minute central *nucleus*, with electrons in the surrounding volume. He received the 1908 Nobel Prize in Chemistry for investigations into the disintegration of the elements and the chemistry of radioactive substances, ironically awarded just as his nuclear atom was taking shape. Later, at the Cavendish, he directed the laboratory in which Chadwick discovered the neutron (1932). Rutherford remains the founding figure of nuclear physics: every scattering formula in this chapter descends, conceptually, from his 1911 insight.

Rutherford's analysis of α-particle scattering established that the positive charge of the atom is concentrated in a tiny central nucleus. As long as the projectile remains outside the range of the nuclear force and samples only the Coulomb field of a point charge Ze, the classical differential cross section is

$$\left(\frac{\mathrm{d}\sigma}{\mathrm{d}\Omega}\right)_{\mathrm{R}} = \left(\frac{Z_1 Z_2 e^2}{8\pi\varepsilon_0\, m v_0^2}\right)^2 \frac{1}{\sin^4(\theta/2)} = \left(\frac{Z_1 Z_2 e^2}{16\pi\varepsilon_0\, E}\right)^2 \frac{1}{\sin^4(\theta/2)}. \tag{1.4}$$

The distance of closest approach for a head-on collision is

$$d_0 = \frac{Z_1 Z_2 e^2}{4\pi\varepsilon_0\, E}, \tag{1.5}$$

and for a general impact parameter the periapsis d and scattering angle are related by

$$d = \frac{d_0}{2}\left(1 + \frac{1}{\sin(\theta/2)}\right). \tag{1.6}$$

When d becomes smaller than a critical value d_N, the measured angular distribution begins to deviate from Equation (1.4). That deviation has two physical origins: (i) the finite spatial extent of the nuclear charge (only charge inside radius d contributes fully to the deflection), and (ii) the onset of the short-range strong interaction.

Historical note: James Chadwick (1891–1974)

Sir James Chadwick studied under Rutherford at Manchester and later worked with Hans Geiger in Berlin before internment in Germany during World War I. Returning to Cambridge, he became Rutherford's close collaborator at the Cavendish. In 1920 he systematically analysed α-particle scattering from a range of targets and helped establish that nuclear radii scale roughly as $A^{1/3}$, the first quantitative size law for nuclei. His lasting fame, however, comes from 1932: interpreting the penetrating radiation that Bothe, Becker, Joliot and Curie had attributed to hard γ-rays, Chadwick showed that it consisted of neutral particles of roughly proton mass: the *neutron*. That discovery completed the proton–neutron picture of the nucleus and earned him the 1935 Nobel Prize in Physics. Without the neutron, the charge densities we extract from electron scattering could not be converted into nucleon densities via A/Z.

Chadwick and later workers analysed such deviations for a series of targets and established the empirical law

$$R_N \simeq r_0\, A^{1/3}, \tag{1.7}$$

with $r_0 \sim 1.3\,\mathrm{fm}$ from α scattering, slightly larger than the electromagnetic value, as expected when the strong force sets the scale [2].

Caution

As θ increases on $(0, \pi)$, $\sin(\theta/2)$ *increases*, so $\csc(\theta/2)$ *decreases*. The Rutherford cross section therefore falls with angle because of $1/\sin^4(\theta/2)$, not because $\sin(\theta/2)$ shrinks. A common slip in lecture notes reverses this statement.

1.2.2 Why electrons?

α particles and protons feel the poorly known nuclear force as soon as they penetrate the surface. Electrons do not: they couple only through the electromagnetic interaction, which is known to exquisite accuracy. High-energy electron scattering, pioneered by Robert Hofstadter and collaborators at Stanford in the 1950s, therefore became the definitive probe of nuclear charge distributions [7, 8, 2].

Historical note: Robert Hofstadter (1915–1990)

Robert Hofstadter was born in New York City and earned his Ph.D. at Princeton (1938) under Louis Ridenour and others, working on photoconductivity and infrared detectors. After wartime radar research and a period at Princeton, he joined Stanford University in 1950 as Associate Professor. There he seized the opportunity offered by the newly available high-energy electron beams from the Stanford linear accelerator (Mark III and related machines). From about 1953 onward, elastic and inelastic electron scattering became his principal research programme.

Directing a high-energy electron beam onto thin targets and measuring the angular distribution of scattered electrons, Hofstadter's group mapped the *charge form factors* of nuclei from light systems (carbon, oxygen) to heavy ones (gold, bismuth), and then of the proton and neutron themselves. The data revealed that nuclei have a roughly constant central density and a diffuse surface (the empirical basis of the Woods–Saxon profile), and that the proton is not a point particle but an extended object of rms radius $\sim 0.8\,\mathrm{fm}$. The term *fermi* (fm) for 10^{-15} m entered common use in this community; Hofstadter himself used it in his 1961 Nobel lecture, "The electron-scattering method and its application to the structure of nuclei and nucleons" (11 December 1961).

He shared the 1961 Nobel Prize in Physics with Rudolf Mössbauer: Hofstadter "for his pioneering studies of electron scattering in atomic nuclei and for his consequent discoveries concerning the structure of nucleons." He remained at Stanford for the rest of his career, was elected to the U.S. National Academy of Sciences (1958), and later received the National Medal of Science (1986). The oxygen data we discuss below (Phys. Rev. **113**, 666, 1959, with Ehrenberg, Meyer-Berkhout, Ravenhall and Sobottka) are a canonical product of that Stanford programme [7, 8].

1.3 The de Broglie condition and the energies required

Historical note: Louis de Broglie (1892–1987)

Prince Louis-Victor de Broglie, of the French noble house of Broglie, was trained first in history before turning to theoretical physics under his brother Maurice and later Paul Langevin. In his 1924 doctoral thesis at the Sorbonne, he proposed that every material particle of momentum p is associated with a wave of wavelength $\lambda = h/p$, extending Einstein's wave–particle duality of light to matter. The idea seemed speculative until Davisson and Germer (1927), and independently G. P. Thomson, observed electron diffraction by crystals, confirming the de Broglie relation experimentally.

De Broglie received the 1929 Nobel Prize in Physics for the discovery of the wave nature of electrons. His relation is the conceptual starting point of this chapter: only when λ_{dB} is of nuclear size (a few fm) can an electron beam resolve the charge distribution inside a nucleus. High-energy electron accelerators are, in that sense, machines built to make de Broglie's wavelength short enough.

Quantum mechanics equips every particle of momentum p with a wavelength

$$\lambda = \frac{h}{p} = \frac{2\pi\hbar}{p} \equiv \lambda_{\mathrm{dB}}. \tag{1.8}$$

Large momentum means short wavelength. For electrons accelerated to kinetic energies well above their rest energy, the kinematics become ultra-relativistic, and the connection between energy and wavelength is especially simple.

1.3.1 Relativistic kinematics

The total energy E of an electron of rest mass m_e and momentum p is

$$E = \sqrt{p^2c^2 + m_e^2c^4}. \tag{1.9}$$

The kinetic energy controlled by the accelerator is the excess over rest energy:

$$K = E - m_ec^2 = \sqrt{p^2c^2 + m_e^2c^4} - m_ec^2. \tag{1.10}$$

Caution

The rest energy is $m_ec^2 \approx 511\,\text{keV}$, *not* $m_e^2c^2$. The latter does not even have the dimension of energy. Always write $K = E - m_ec^2$.

For electrons, once $K \gg m_ec^2$—true already at a few tens of MeV—the rest mass may be neglected and

$$E \approx K \approx pc. \tag{1.11}$$

The de Broglie wavelength then collapses to

$$\lambda_{\text{dB}} \approx \frac{hc}{E} = \frac{2\pi\,\hbar c}{E}. \tag{1.12}$$

In nuclear units the conversion constants

$$hc \approx 1240\,\text{MeV}\cdot\text{fm}, \qquad \hbar c \approx 197.3\,\text{MeV}\cdot\text{fm} \tag{1.13}$$

are indispensable. Thus, to resolve structure on the scale of 10 fm,

$$E \approx \frac{1240\,\text{MeV}\cdot\text{fm}}{10\,\text{fm}} = 124\,\text{MeV}. \tag{1.14}$$

Example: electrons at 500 MeV

For $E = 500\,\text{MeV}$ one has $\lambda_{\text{dB}} \approx 2.48\,\text{fm}$, already small compared with the diameter of a heavy nucleus [2]. Using Equation (1.12),

$$\lambda_{\text{dB}} \approx \frac{1240\,\text{MeV}\cdot\text{fm}}{500\,\text{MeV}} = 2.48\,\text{fm}, \qquad \bar{\lambda} = \frac{\hbar c}{E} \approx 0.395\,\text{fm}.$$

The two numbers describe different, explicitly named quantities; they must not both be called λ.

Key idea

For phase resolution, choose a momentum transfer $q \gtrsim \hbar/\ell$; for the stricter full-wavelength criterion use $p \gtrsim h/\ell$. Thus resolving $\ell \sim 1\,\text{fm}$ requires momentum transfers of a few hundred MeV/c, while $\lambda_{\text{dB}} \lesssim 1\,\text{fm}$ requires $E \sim 1.2\,\text{GeV}$. Modern facilities (Jefferson Lab, MAMI, formerly SLAC) operate comfortably in this regime.

1.4 Elastic electron scattering: the oxygen example

A classic data set is the elastic scattering of 420 MeV electrons from oxygen, shown in Figure 1.2 [8, 7].

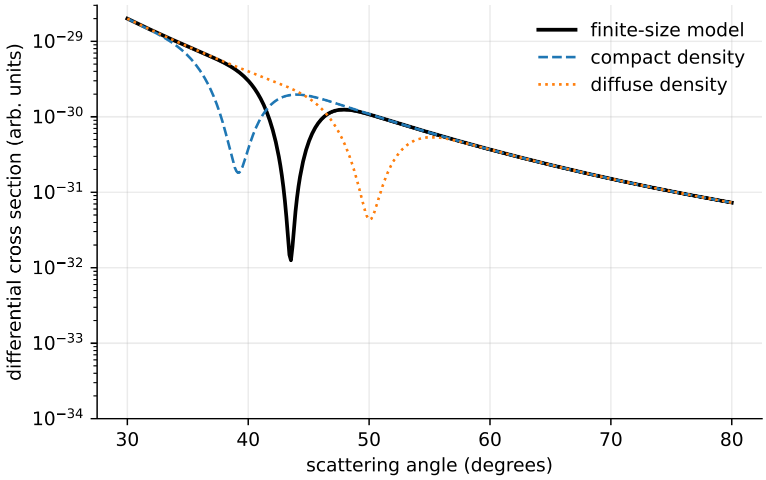

Figure 1.2: Differential cross section for elastic electron scattering from oxygen at 420 MeV, compared with harmonic-well charge distributions (a)–(c). The data display a clear diffraction minimum near 43°–44°. Original redraw of the trend in Ehrenberg et al., Phys. Rev. **113**, 666 (1959); the model curves are schematic rather than digitised data.

What does one actually measure? A beam of monoenergetic electrons strikes a thin target. Detectors placed at laboratory angle θ count the scattered electrons. The observable is the differential cross section $d\sigma/d\Omega$, proportional to the number of electrons scattered into a solid angle $d\Omega$ about θ.

Two features of Figure 1.2 are immediate.

1. **Overall fall-off.** The cross section drops by several orders of magnitude as θ increases from $\sim 30°$ to $\sim 80°$.

2. **Diffraction structure.** Superimposed on the fall-off is a deep minimum near 43°–44°, followed by a secondary maximum and a further decline.

The first feature is the relativistic generalisation of Rutherford scattering (Mott scattering for Dirac electrons). The second is the fingerprint of a finite nuclear size: diffraction of the electron wave by an extended charge distribution. Before developing that analogy, two experimental points deserve emphasis.

1.4.1 Selecting nuclear, not electronic, scattering

An oxygen target contains both a nucleus and eight atomic electrons. An incident electron can scatter from either. Scattering from an atomic electron transfers a large fraction of the beam energy (comparable masses in a nearly elastic collision), so the scattered electron emerges with substantially reduced energy. Scattering from the much heavier nucleus is essentially elastic: the recoiling nucleus takes little kinetic energy, and the scattered electron retains nearly its full beam energy.

Remark

In the laboratory one therefore applies an energy cut, retaining only events with $E' \approx E_{\text{beam}}$. That cut isolates elastic *nuclear* scattering and rejects the electron–electron background. The data of Figure 1.2 are of this elastic character.

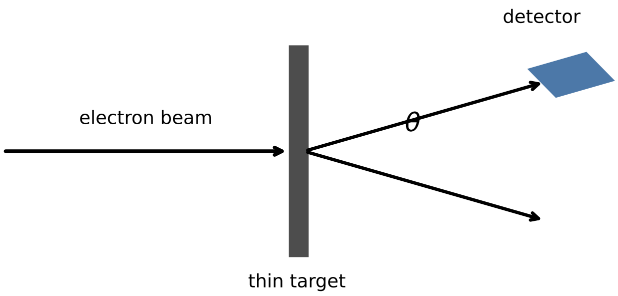

Figure 1.3: Left: schematic of an electron beam scattering from a thin sample into a detector at angle θ. Right: qualitative angular dependence of the detector reading, with a diffraction minimum at θ_{min}.

Even the Rutherford formula is not quantitatively applicable at 420 MeV. Electrons are ultra-relativistic ($E/m_e c^2 \sim 800$), so the proper point-charge baseline is the *Mott* cross section, the Dirac generalisation of Rutherford scattering. Finite nuclear size then multiplies the Mott result by the square of a form factor (Section 1.6).

Historical note: Nevill F. Mott (1905–1996)

Sir Nevill Francis Mott was one of the leading theoretical physicists of the twentieth century. Educated at Clifton College and St John's College, Cambridge, he worked in Copenhagen and Göttingen in the early years of quantum mechanics before returning to the United Kingdom. In 1929–1930, applying Dirac's relativistic theory of the electron to Coulomb scattering, he derived the cross section for a point charge that now bears his name: the *Mott formula.* It reduces to Rutherford scattering in the non-relativistic limit, but at high energy it includes spin and relativistic kinematics and becomes the natural baseline for electron–nucleus experiments.

Mott's career ranged far beyond nuclear scattering: he made foundational contributions to solid-state physics (metal–insulator transitions, the Mott insulator), shared the 1977 Nobel Prize in Physics with P. W. Anderson and J. H. Van Vleck for electronic structure of magnetic and disordered systems, and served as Cavendish Professor at Cambridge. In the present chapter, whenever we write $(\mathrm{d}\sigma/\mathrm{d}\Omega)_{\text{Mott}}$, we are using the point-charge Dirac result he obtained almost a century ago, the yardstick against which finite-size form factors are measured.

1.5 Diffraction analogy and a first estimate of the nuclear size

The diffraction minimum in Figure 1.2 is the nuclear counterpart of a familiar optical effect. Consider monochromatic, coherent light of wavelength λ incident on a single slit of width b (Figure 1.4). On a distant screen the intensity is

$$I(\theta) = I_0 \left(\frac{\sin\beta}{\beta}\right)^2, \qquad \beta = \frac{\pi b \sin\theta}{\lambda}. \tag{1.15}$$

The intensity vanishes whenever $\beta = m\pi$ for nonzero integer m, i.e. whenever

$$b \sin\theta = m\lambda, \qquad m = \pm 1, \pm 2, \dots \tag{1.16}$$

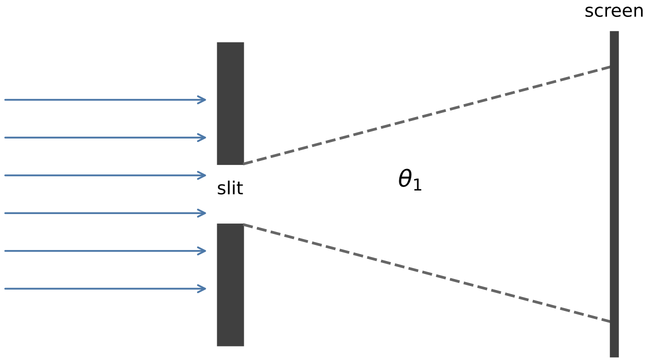

Figure 1.4: Geometry of single-slit diffraction. Plane waves of wavelength λ pass through a slit of width b and form an interference pattern on a distant screen ($L \gg b$). Intensity minima occur near $y_m = m\,\lambda L/b$ for integer $m \neq 0$.

For a *circular* aperture of diameter D, the first dark ring of the Airy pattern sits at

$$\sin\theta = \frac{1.22\,\lambda}{D}. \tag{1.17}$$

Treating the nucleus, very roughly, as a circular obstacle of diameter D, one may invert Equation (1.17) to estimate D from the observed diffraction minimum. Equivalently, the first minimum is often written condition as $\theta_{\rm min} \approx \lambda_{\rm dB}/D$ (in radians, for small angles), corresponding to a path difference of half a wavelength between opposite edges of the charge distribution [2].

Example: oxygen at 420 MeV

At $E = 420\,\mathrm{MeV}$,

$$\lambda \approx \frac{hc}{E} \approx \frac{1240\,\mathrm{MeV}\cdot\mathrm{fm}}{420\,\mathrm{MeV}} \approx 3.0\,\mathrm{fm}.$$

The first minimum in the oxygen data lies near $\theta \approx 45^\circ$. Equation (1.17) then yields

$$D = \frac{1.22\,\lambda}{\sin\theta} \approx \frac{1.22 \times 3.0\,\mathrm{fm}}{\sin 45^\circ} = \frac{1.22 \times 3.0\,\mathrm{fm}}{1/\sqrt{2}} \approx 5.2\,\mathrm{fm}.$$

The corresponding radius, $R = D/2 \approx 2.6\,\mathrm{fm}$, is a respectable first estimate for ^{16}O. The empirical rule $R \approx 1.2\,\mathrm{fm}\,A^{1/3}$ with $A = 16$ gives $R \approx 3.0\,\mathrm{fm}$—the same order of magnitude.

Remark

This optical analogy is intentionally crude. The nucleus is not a hard disk with a sharp edge; the electron is a charged Dirac particle, not a scalar optical wave; and the Coulomb field extends beyond the nuclear surface. A proper treatment replaces the slit formula by a Fourier transform of the charge density (the form factor). The estimate nonetheless shows that the angular location of the first diffraction minimum is a direct ruler for the nuclear size. As the beam energy rises, λ falls and the first minimum moves to smaller angles [2], exactly as seen in multi-energy data for gold and other targets.

Why is only one minimum visible in the oxygen data? For a second minimum one would need $b\sin\theta = 2\lambda$, or $\sin\theta = 2\lambda/D$. With $D \approx 5.2\,\text{fm}$ and $\lambda \approx 3\,\text{fm}$ that ratio exceeds unity: no real angle exists. Heavier nuclei (larger D) or higher beam energies (smaller λ) push λ/D down and bring additional diffraction minima into the physical domain. Lead or gold at hundreds of MeV to GeV energies display a rich oscillatory pattern; the number of observed minima tracks the zeros of the form factor of a uniform sphere [3].

1.6 From diffraction to charge density: the form factor

Electron scattering can do more than estimate a single radius. Because the interaction is electromagnetic and weak compared with the nuclear binding scale (at moderate momentum transfers), the Born approximation is an excellent starting point for light nuclei. The scattering amplitude then becomes proportional to the Fourier transform of the nuclear charge density: the *charge form factor*.

1.6.1 Plane-wave Born picture

Write the initial and final electron waves as plane waves of physical momenta $\boldsymbol{p}$ and $\boldsymbol{p}'$ (Coulomb distortion is discussed below):

$$\psi_i(\boldsymbol{r}) = e^{i\boldsymbol{p}\cdot\boldsymbol{r}/\hbar}, \qquad \psi_f(\boldsymbol{r}) = e^{i\boldsymbol{p}'\cdot\boldsymbol{r}/\hbar}. \tag{1.18}$$

For elastic scattering $|\boldsymbol{p}| = |\boldsymbol{p}'| \equiv p$; only the direction changes. Define the physical three-momentum transfer $\boldsymbol{q} = \boldsymbol{p} - \boldsymbol{p}'$. Squaring,

$$\begin{aligned} q^2 = |\boldsymbol{p} - \boldsymbol{p}'|^2 &= p^2 + p^2 - 2\boldsymbol{p}\cdot\boldsymbol{p}' = 2p^2(1-\cos\theta) \\ &= 4p^2\sin^2(\theta/2), \end{aligned} \tag{1.19}$$

where the last step uses the half-angle identity $1 - \cos\theta = 2\sin^2(\theta/2)$. Therefore

$$\boldsymbol{q} = \boldsymbol{p} - \boldsymbol{p}', \qquad q = |\boldsymbol{q}| = 2p\sin(\theta/2). \tag{1.20}$$

The corresponding wave-vector transfer is $\Delta k = \boldsymbol{q}/\hbar$. Throughout this chapter q has momentum units; every Fourier phase therefore contains $qr/\hbar$.

The electron couples to the nuclear charge density $\rho(\boldsymbol{r}')$ through the Coulomb interaction. The perturbation may be written

$$H' = \int \rho(\boldsymbol{r}')\,\frac{-e}{4\pi\varepsilon_0\,|\boldsymbol{r} - \boldsymbol{r}'|}\,\mathrm{d}\tau'. \tag{1.21}$$

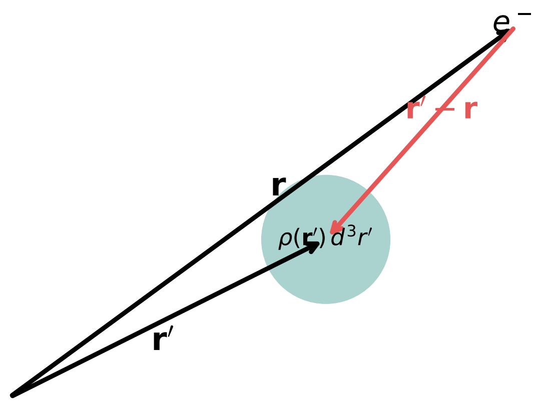

Figure 1.5: Geometry of the Coulomb interaction. An electron at $\boldsymbol{r}$ interacts with a nuclear charge element $\rho(\boldsymbol{r}')\,\mathrm{d}\tau'$ at $\boldsymbol{r}'$. The relative vector is $\boldsymbol{r}' - \boldsymbol{r}$; $\mathrm{d}\tau'$ is a nuclear volume element.

In first-order perturbation theory the transition amplitude is

$$\mathcal{M}_{fi} = \int \psi_f^*(\boldsymbol{r})\,H'\,\psi_i(\boldsymbol{r})\,\mathrm{d}\tau. \tag{1.22}$$

Substitute the plane waves and (1.21):

$$\begin{aligned}\mathcal{M}_{fi} &= \int \mathrm{d}\tau\, e^{-i\boldsymbol{k}'\cdot\boldsymbol{r}} \left[\int \mathrm{d}\tau'\,\rho(\boldsymbol{r}')\,\frac{-e}{4\pi\varepsilon_0\,|\boldsymbol{r}-\boldsymbol{r}'|}\right] e^{i\boldsymbol{k}\cdot\boldsymbol{r}} \\ &= \int \mathrm{d}\tau'\,\rho(\boldsymbol{r}') \left[\int \mathrm{d}\tau\,\frac{-e}{4\pi\varepsilon_0\,|\boldsymbol{r}-\boldsymbol{r}'|}\,e^{i\boldsymbol{q}\cdot\boldsymbol{r}/\hbar}\right],\end{aligned} \tag{1.23}$$

with $\boldsymbol{q} = \boldsymbol{p} - \boldsymbol{p}'$. The inner integral is the Fourier transform of the Coulomb kernel. Shifting $\boldsymbol{s} = \boldsymbol{r} - \boldsymbol{r}'$ shows that it equals

$$e^{i\boldsymbol{q}\cdot\boldsymbol{r}'/\hbar}\int \frac{-e}{4\pi\varepsilon_0\,s}\,e^{i\boldsymbol{q}\cdot\boldsymbol{s}/\hbar}\,\mathrm{d}^3 s = e^{i\boldsymbol{q}\cdot\boldsymbol{r}'/\hbar}\left(\frac{-e\hbar^2}{\varepsilon_0\,q^2}\right)$$

(in the convention where $\int e^{i\boldsymbol{q}\cdot\boldsymbol{s}/\hbar}/s\,\mathrm{d}^3 s = 4\pi\hbar^2/q^2$). Thus

$$\mathcal{M}_{fi} = \underbrace{\left(-\frac{e\hbar^2}{\varepsilon_0\,q^2}\right)}_{\text{point Coulomb / Mott kinematics}} \int \rho(\boldsymbol{r}')\,e^{i\boldsymbol{q}\cdot\boldsymbol{r}'/\hbar}\,\mathrm{d}\tau'. \tag{1.24}$$

The amplitude therefore factorises into a known kinematic piece times the Fourier transform of the charge density.

Definition: charge form factor

$$F(\boldsymbol{q}) = \frac{1}{Ze}\int \rho(\boldsymbol{r}')\, e^{i\boldsymbol{q}\cdot\boldsymbol{r}'/\hbar}\,\mathrm{d}\tau', \qquad F(0) = 1. \tag{1.25}$$

For a spherical ground state $\rho = \rho(r)$ only, choose the polar axis along $\boldsymbol{q}$ so that $\boldsymbol{q}\cdot\boldsymbol{r}' = qr\cos\theta'$. Then

$$\begin{aligned} F(q) &= \frac{1}{Ze}\int_0^\infty \rho(r)\, r^2\,\mathrm{d}r \int_0^{2\pi}\mathrm{d}\phi' \int_{-1}^{1}\mathrm{d}(\cos\theta')\, e^{iqr\cos\theta'/\hbar} \\ &= \frac{4\pi}{Ze}\int_0^\infty \rho(r)\,\frac{\sin(qr/\hbar)}{qr/\hbar}\, r^2\,\mathrm{d}r, \end{aligned} \tag{1.26}$$

because $\int_{-1}^{1} e^{ix\cos\theta}\,\mathrm{d}(\cos\theta) = 2\sin x/x$. Equivalently, writing the Fourier transform of a normalised charge density [2],

$$F(\Delta k) = \int \rho_e(\boldsymbol{r})\, e^{i\Delta k\cdot\boldsymbol{r}}\,\mathrm{d}^3 r, \qquad \Delta k = \boldsymbol{q}/\hbar,$$

(up to normalisation by the total charge Ze).

The measured cross section factors as

$$\frac{\mathrm{d}\sigma}{\mathrm{d}\Omega} = \left(\frac{\mathrm{d}\sigma}{\mathrm{d}\Omega}\right)_{\text{point}} |F(q)|^2, \tag{1.27}$$

where the point-charge baseline is the Rutherford (non-relativistic) or Mott (relativistic Dirac) formula. All information about the spatial distribution of charge resides in $F(q)$. The momentum transfer that enters the Fourier phase has magnitude

$$q = |\boldsymbol{q}| = 2p\sin(\theta/2) \tag{1.28}$$

for elastic scattering at beam momentum p [1].

Caution

The form factor is defined as the ratio of the full scattering amplitude to the point-charge (Rutherford/Mott) amplitude, so that the Coulomb $1/q^2$ factors cancel by construction [6, 1]. Do not confuse $F(q)$ with the full Born amplitude, which still contains the photon propagator. Also keep the matrix-element convention consistent: $\mathcal{M}_{fi} = \langle f|H'|i\rangle$ with the final wave conjugated, and a fixed sign for $\boldsymbol{q} = \boldsymbol{k} - \boldsymbol{k}'$.

Key idea

Measuring $\mathrm{d}\sigma/\mathrm{d}\Omega$ as a function of angle (hence of q) determines $|F(q)|$. One may then either (i) extract $\rho(r)$ by a model-independent numerical inversion, or (ii) assume a parametric Woods–Saxon shape and fit its parameters to the data [1]. Both routes are used in practice; the parametric form is convenient for nuclear-model calculations.

Example: uniform sphere

For a uniform charge distribution of radius R_A,

$$\rho(r) = \begin{cases} \dfrac{Ze}{\frac{4}{3}\pi R_A^3}, & r \le R_A, \\ 0, & r > R_A. \end{cases}$$

Equation (1.26) becomes

$$F(q) = \frac{4\pi}{Ze}\,\frac{Ze}{\frac{4}{3}\pi R_A^3}\int_0^{R_A}\frac{\sin(qr/\hbar)}{qr/\hbar}\,r^2\,\mathrm{d}r = \frac{3}{R_A^3}\int_0^{R_A} r^2\,\frac{\sin(qr)}{qr}\,\mathrm{d}r. \tag{1.29}$$

Integrate by parts (or use $j_1(x) = \sin x/x^2 - \cos x/x$) with $x = qR_A/\hbar$:

$$F(q) = \frac{3}{(qR_A/\hbar)^3}\left[\sin(qR_A/\hbar) - (qR_A/\hbar)\cos(qR_A/\hbar)\right] = \frac{3j_1(qR_A/\hbar)}{qR_A/\hbar}. \tag{1.30}$$

The zeros of j_1 fix the diffraction minima. The first zero of $j_1(x) = 0$ solves $\tan x = x$ and lies at $x \approx 4.493$, so $q_1 R_A/\hbar \approx 4.49$; counting zeros at fixed energy is a quick estimate of R_A [3].

For any spherical density the small-q expansion follows from $\sin(qr/\hbar)/(qr/\hbar) = 1 - q^2r^2/(6\hbar^2) + \cdots$:

$$\begin{aligned} F(q) &= \frac{4\pi}{Ze}\int_0^\infty \rho(r)\left(1 - \frac{q^2r^2}{6\hbar^2} + \cdots\right)r^2\,\mathrm{d}r \\ &= 1 - \frac{q^2}{6\hbar^2}\langle r^2\rangle + \cdots, \end{aligned} \tag{1.31}$$

where $\langle r^2\rangle = (1/Ze)\int \rho(r)\,r^2\,\mathrm{d}^3r$. Thus the slope of $F(q)$ at the origin determines the rms charge radius without assuming a full density model. For the uniform sphere, $\langle r^2\rangle = \frac{3}{5}R_A^2$.

Coulomb distortion and heavy nuclei

At low energy, or for heavy nuclei ($Z\alpha$ not small), plane waves are a poor description of the electron in the nuclear Coulomb field. One then solves the Dirac equation in the electrostatic potential of a trial $\rho(r)$ (phase-shift / distorted-wave analysis) and adjusts ρ until the calculated cross section matches experiment. The qualitative content of Equation (1.27) survives; quantitative extractions for ^{208}Pb or ^{197}Au require this treatment [2].

1.7 Empirical charge densities: the Woods–Saxon profile

Once form-factor data are inverted, a remarkably simple picture emerges. Figure 1.6 shows proton (charge) densities for three representative nuclei: ^{16}O, ^{118}Sn, and ^{197}Au. Hofstadter's classic compilation for a broader range of nuclei (H through Bi) shows the same pattern [2]: a flat interior and a diffuse surface.

Several features are universal enough to deserve names.

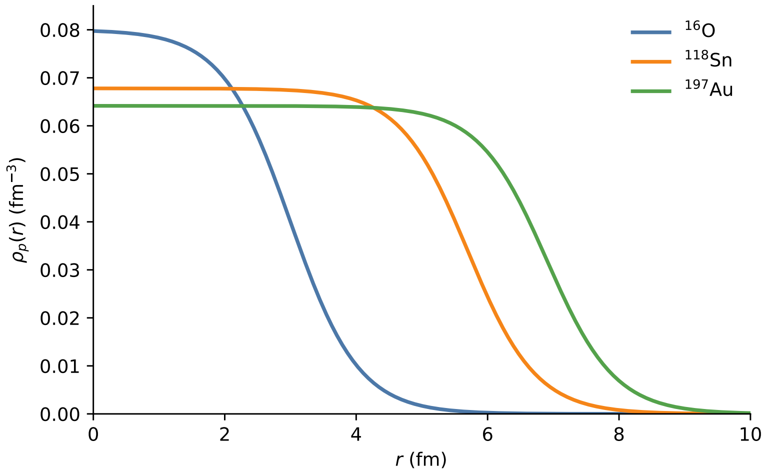

Figure 1.6: Woods–Saxon charge distributions for ^{16}O, ^{118}Sn, and ^{197}Au. The proton density $\rho_p(r)$ is nearly flat in the nuclear interior and falls smoothly through the surface. Heavier systems have larger half-density radii and slightly lower central charge densities.

1. **A flat interior.** From the centre out to a few fermis, $\rho_p(r)$ is roughly constant. Nuclei are not hollow; charge fills the volume.
2. **A diffuse surface.** The density does not terminate abruptly. It falls from $\sim 90\%$ to $\sim 10\%$ of its central value over a surface thickness of order 2.5 fm.
3. **Larger systems, larger radii.** The half-density radius grows with mass number, consistent with $R \propto A^{1/3}$.
4. **Mild A-dependence of the central charge density.** Lighter nuclei show a somewhat higher central ρ_p; heavier nuclei are slightly lower, consistent with Coulomb repulsion pushing protons outward. When one forms the *nucleon* density by scaling $\rho_A(r) \approx (A/Z)\,\rho_p(r)$, the central values collapse to a nearly universal $\rho_0 \approx 0.16 - -0.17\,1/\text{fm}^3$.

Historical note: R. D. Woods and D. S. Saxon

The functional form that now bears their names was introduced in 1954 by **Roger D. Woods** and **David S. Saxon** at the University of California, Los Angeles, in a Physical Review paper on the elastic scattering of 20 MeV protons (Phys. Rev. **95**, 577, 1954). They needed a smooth, finite-range mean-field potential that was roughly constant in the nuclear interior and fell to zero over a surface of finite thickness: neither a pure square well nor an infinite oscillator. The form

$$V(r) = -\frac{V_0}{1 + \exp\big[(r - R)/a\big]}$$

did the job, and it quickly became the standard phenomenological optical and shell-model potential.
The same shape describes the empirical *charge density* extracted from electron scattering: a flat bulk and a diffuse surface. In the literature one meets both "Woods–Saxon" and "Saxon–Woods"; both refer to this two-parameter Fermi profile. Saxon later contributed broadly to nuclear reaction theory and computing in physics; the potential remains one of the most-cited phenomenological tools in nuclear structure.

Definition: Woods–Saxon (two-parameter Fermi) density

$$\rho(r) = \frac{\rho_0}{1 + \exp\big[(r - R)/a\big]}. \tag{1.32}$$

Here ρ_0 is the central density, R is the half-density radius ($\rho(R) = \rho_0/2$), and a is the diffuseness. The surface thickness t (distance from 90% to 10% of ρ_0) is related to a by

$$t = 4a \ln 3 \approx 4.40\, a. \tag{1.33}$$

A global analysis of scattering data finds that a is essentially independent of mass number,

$$a = 0.52\,\text{fm} \pm 0.01\,\text{fm}, \tag{1.34}$$

so the surface thickness is $t = 4a \ln 3 \approx 2.3\,\text{fm}$ [1]. The same functional form appears as the Woods–Saxon (or Saxon–Woods) mean field in the nuclear shell model [3, 4, 1].

What the charge densities show [1]

Comparing Woods–Saxon charge profiles for light and heavy nuclei one finds three regularities:

1. Larger nuclei have a larger half-density radius.
2. The surface width a (hence t) is nearly the same for all A.
3. The *central charge* density is higher in light nuclei than in heavy ones (Coulomb repulsion pushes protons outward as Z grows).

After rescaling to nucleon density by A/Z (Lecture 2), the central *nucleon* density becomes nearly universal.

Caution

Electrons couple to electric charge. What Figure 1.6 shows is therefore the *proton* (charge) density $\rho_p(r)$, not the full nucleon density. Neutrons are electromagnetically nearly invisible to ordinary (parity-conserving) electron scattering. The rescaling $\rho_A \approx (A/Z)\,\rho_p$ assumes similar proton and neutron profiles (reasonable for $N \approx Z$, increasingly questionable for heavy, neutron-rich systems).

1.7.1 Several definitions of "the" nuclear radius

Because the surface is diffuse, there is no unique nuclear radius. Three common definitions, following [2], are:

- R_m: radius at which the density has fallen to half its central value (the Woods–Saxon R).
- R_N: radius at which the density has essentially vanished (a practical outer edge).
- $R_{1/2}$: a half-density radius defined on a particular model of the edge.

They differ by $\sim 10--20\,\%$ and all scale roughly as $A^{1/3}$. The volume per nucleon implied by these radii lies in the range $\sim 4--9\,\mathrm{fm}^3$, corresponding to the saturation density above.

1.7.2 Charge radius and the $A^{1/3}$ law

Electron scattering determines not only the shape of $\rho(r)$ but also moments. The most frequently quoted is the root-mean-square (rms) charge radius,

$$\langle r^2\rangle_{\mathrm{ch}}^{1/2} = \left(\frac{1}{Ze}\int r^2\,\rho(r)\,\mathrm{d}\tau\right)^{1/2}. \tag{1.35}$$

For a uniform sphere of radius R one has $\langle r^2\rangle^{1/2} = \sqrt{3/5}\,R$; the Woods–Saxon surface corrects this at the few-percent level. From the low-q expansion Equation (1.31),

$$\langle r^2\rangle = -6\,\hbar^2 \frac{\mathrm{d}F}{\mathrm{d}(q^2)}\bigg|_{q=0}, \tag{1.36}$$

so a careful measurement of $F(q)$ near the origin yields the rms radius model-independently. Empirically, the half-density (or equivalent hard-sphere) radius follows [1]

$$R_0 = 1.2\,\mathrm{fm}\times A^{1/3}. \tag{1.37}$$

This is exactly what one expects for systems of different mass but the *same* bulk density: volume $\propto A$ implies radius $\propto A^{1/3}$. Equation (1.37) is a central input to the liquid-drop model developed in later chapters.

Example: ^{12}C radius from form-factor data [3]

Expanding $F(q)$ at low q and fitting measured cross sections for ^{12}C yields $\langle r^2\rangle^{1/2} \approx 2.44\,\mathrm{fm}$ for a uniform-sphere equivalent radius, consistent with $r_0 A^{1/3}$ at $A = 12$.

1.7.3 Which feature of $F(q)$ constrains which property?

The form-factor programme answers three nested questions about $\rho_{\mathrm{ch}}(r)$:

Observable in $F(q)$	Density property	Typical scale
Low-q slope of F	$\langle r^2\rangle_{\mathrm{ch}}$	$r_{\mathrm{rms}} \sim 2$–$6\,\mathrm{fm}$
Location of diffraction minima	Overall size R	$R \approx 1.2\,A^{1/3}\,\mathrm{fm}$
Depth / washing of minima	Surface diffuseness a (skin t)	$a \approx 0.52\,\mathrm{fm}$, $t \approx 2.3\,\mathrm{fm}$

A sharp sphere produces deep zeros of $j_1(qR)$; a diffuse Woods–Saxon surface softens those minima but does not erase the $A^{1/3}$ growth of R [6, 1, 7]. Lecture 2 will convert the same profiles into a saturated *matter* density.

Takeaway

The Woods–Saxon profile encodes two great empirical facts of nuclear bulk structure: **saturation** (a constant central density of order $0.16/\mathrm{fm}^3$) and a **surface of nearly universal thickness** ($t \approx 2.3\,\mathrm{fm}$). Both reappear in the liquid-drop model, the nuclear equation of state, and the neutron skins of heavy nuclei.

1.8 What electrons do not see: neutrons and skins

Electrons couple to electric charge. In a nucleus, charge resides on protons (up to small meson-exchange and spin-orbit contributions). The neutron distribution $\rho_n(r)$ is invisible to ordinary electron scattering.

In light, $N = Z$ nuclei one may reasonably assume $\rho_n \approx \rho_p$. In heavy nuclei, where $N > Z$, a neutron skin develops: the neutron distribution extends farther than the proton distribution. The skin thickness

$$\Delta r_{np} = \langle r^2 \rangle_n^{1/2} - \langle r^2 \rangle_p^{1/2} \tag{1.38}$$

is a laboratory observable with a direct link to the density dependence of the nuclear symmetry energy, and, through that link, to the radii of neutron stars. Measuring Δr_{np} requires either hadronic probes (with their attendant model dependence) or parity-violating electron scattering, in which the Z^0 boson couples preferentially to neutrons. That programme (PREX, CREX, and their successors) lies beyond this chapter, but the conceptual foundation has been laid: once the proton distribution is known, the neutron distribution becomes the next frontier.

Remark

Complementary probes of the charge distribution include muonic atoms: because $m_\mu \approx 207\,m_e$, the muonic Bohr radius is ~ 200 times smaller than the electronic one, so the muon wave function overlaps the nucleus strongly and level shifts are sensitive to $\langle r^2 \rangle_{\mathrm{ch}}$ [2]. Lecture 3 develops that finite-size spectroscopy in detail.

1.9 Summary and outlook

- Nuclear sizes are a few fermis. Probing them requires electron energies of hundreds of MeV so that $\lambda \lesssim R$.
- Rutherford/Chadwick α scattering first established $R \propto A^{1/3}$; Hofstadter electron scattering mapped the full charge density.
- Elastic electron scattering measures a diffraction pattern whose first minimum already yields a crude nuclear diameter, and whose full angular distribution determines the charge form factor $F(q)$.
- In the Born approximation, $\mathrm{d}\sigma/\mathrm{d}\Omega = (\mathrm{d}\sigma/\mathrm{d}\Omega)_{\mathrm{Mott}}\,|F(q)|^2$, with $F(q)$ the Fourier transform of $\rho(r)$.
- Empirical densities are well described by a Woods–Saxon profile: flat interior, diffuse surface of nearly universal thickness, and radius scaling as $A^{1/3}$.

- Electrons map protons. Neutrons (and with them the symmetry energy and the neutron-star connection) require additional probes.

Next. Lecture 2 converts charge density to mass density and explains saturation ($R \propto A^{1/3}$, short-range force). Lecture 3 then remeasures the same radii through atomic and muonic finite-size shifts.

1.10 Deeper physics: Mott baseline and reading $F(q)$

1.10.1 Rutherford / Mott baseline and finite-size reduction

For a point Coulomb centre the orbit itself supplies the cross section. Let

$$a = \frac{Zze^2}{4\pi\varepsilon_0}, \qquad E = \frac{1}{2}mv_0^2.$$

Conservation of energy and angular momentum for a repulsive hyperbolic orbit gives the impact-parameter relation

$$b = \frac{a}{2E}\cot\frac{\theta}{2}. \tag{1.39}$$

An azimuthally symmetric beam maps the incident annulus $2\pi b\,\mathrm{d}b$ into the solid angle $\mathrm{d}\Omega = 2\pi\sin\theta\,|\mathrm{d}\theta|$. Hence

$$\begin{aligned}\frac{\mathrm{d}\sigma}{\mathrm{d}\Omega} &= \frac{b}{\sin\theta}\left|\frac{\mathrm{d}b}{\mathrm{d}\theta}\right| = \left(\frac{a}{4E}\right)^2\csc^4\frac{\theta}{2}\\ &= \left(\frac{Zze^2}{16\pi\varepsilon_0 E}\right)^2\csc^4\frac{\theta}{2}.\end{aligned} \tag{1.40}$$

Using $mv_0^2 = 2E$, this is equivalently

$$\frac{\mathrm{d}\sigma}{\mathrm{d}\Omega} = \left(\frac{Zze^2}{8\pi\varepsilon_0 mv_0^2}\right)^2\csc^4\frac{\theta}{2} \tag{1.41}$$

for non-relativistic projectiles of charge ze on a nucleus of charge Ze. A full quantum treatment of a pure $1/r$ potential reproduces the same result.

For a relativistic spin-$\frac{1}{2}$ electron, evaluating the Dirac current in the first Born approximation multiplies the spinless point-charge result by $1-\beta^2\sin^2(\theta/2)$. Neglecting nuclear recoil,

$$\left(\frac{\mathrm{d}\sigma}{\mathrm{d}\Omega}\right)_{\text{Mott}} = \left(\frac{Z\alpha\hbar c}{2pv}\right)^2\frac{1-\beta^2\sin^2(\theta/2)}{\sin^4(\theta/2)}, \qquad \beta = \frac{v}{c}. \tag{1.42}$$

For $E \simeq pc$ and $\beta \simeq 1$, this becomes

$$\left(\frac{\mathrm{d}\sigma}{\mathrm{d}\Omega}\right)_{\text{Mott}} \simeq \left(\frac{Z\alpha\hbar c}{2E}\right)^2\frac{\cos^2(\theta/2)}{\sin^4(\theta/2)}.$$

The factor $\cos^2(\theta/2)$ is the helicity/spin correction; the remaining $\csc^4(\theta/2)$ is the Rutherford angular skeleton. Finite nuclear size then multiplies the appropriate point baseline by a form factor:

$$\left(\frac{\mathrm{d}\sigma}{\mathrm{d}\Omega}\right)_{\mathrm{exp}} = \left(\frac{\mathrm{d}\sigma}{\mathrm{d}\Omega}\right)_{\mathrm{point}} |F(\boldsymbol{q})|^2, \tag{1.43}$$

with $F(0) = 1$. At every nonzero angle, $|F|^2 < 1$: the nucleus is a softer scatterer than a point charge of the same Z [6, 1].

1.10.2 From $|F|^2$ back to $\rho_{\mathrm{ch}}(r)$

In the plane-wave Born approximation,

$$F(q) = \frac{1}{Ze}\int \rho_p(\boldsymbol{r})\, e^{i\boldsymbol{q}\cdot\boldsymbol{r}/\hbar}\, \mathrm{d}^3r, \qquad q = 2p\sin(\theta/2). \tag{1.44}$$

A practical inversion pipeline is:

1. Divide the measured $\mathrm{d}\sigma/\mathrm{d}\Omega$ by the Mott (point) prediction to obtain $|F(q)|^2$.
2. Fit a parametric density (Woods–Saxon, or a model-independent Fourier–Bessel expansion) so that its Fourier transform matches $F(q)$ over the measured q range.
3. Quote moments: $\langle r^2\rangle$ from the low-q curvature; R and a from the full pattern.

Diffraction minima at larger q constrain the surface diffuseness and possible shell oscillations in $\rho(r)$ [6, 1, 7].

Worked reading of a diffraction minimum

For a uniform sphere, the first zero of $j_1(qR)$ sits near $qR \approx 4.49$. With $q = 2p\sin(\theta/2)$ at fixed beam momentum, a measured first-minimum angle therefore returns R. Replacing the sharp edge by a Woods–Saxon skin of thickness $t \approx 2.3\,\mathrm{fm}$ fills in the zero partially but hardly moves its angular location: size and diffuseness play distinct roles in $F(q)$, as in Section 1.7.3.

Key idea

What Hofstadter measured. Not a single radius, but a function $\rho_{\mathrm{ch}}(r)$: central plateau, surface of thickness $\sim 2.3\,\mathrm{fm}$, and $R \propto A^{1/3}$. Form-factor zeros move to smaller angles as beam energy rises (de Broglie wavelength shrinks), exactly as in optical diffraction from a larger aperture relative to λ.

1.11 Physics depth: diffraction scale of $F(q)$

The Mott baseline of Lecture 1 tells you the cross section for a *point* charge. Every measured reduction $|F(q)|^2 < 1$ is therefore a statement about extended charge. The momentum transfer $q = (2E/c)\sin(\theta/2)$ (ultra-relativistic limit) is the ruler: when $qR \sim \pi$, the Fourier transform of a compact charge distribution develops its first diffraction minimum.

1.11.1 Worked estimate: first zero for a uniform sphere

For a sharp sphere of radius R,

$$F(q) = \frac{3j_1(qR)}{qR}, \qquad j_1(x) = \frac{\sin x - x\cos x}{x^2}. \tag{1.45}$$

The first nontrivial zero of j_1 sits near $qR \simeq 4.49$. Taking $R = 1.2\,A^{1/3}\,\mathrm{fm}$ for $^{12}\mathrm{C}$ gives $R \simeq 2.7\,\mathrm{fm}$, so

$$q_{\min} \simeq \frac{4.49}{R} \simeq 1.7\,\mathrm{fm}^{-1}.$$

At $E = 500\,\mathrm{MeV}$ one has $q \simeq (5.07\,\mathrm{fm}^{-1})\sin(\theta/2)$, hence $\theta_{\min} \sim 40°$. Raising E moves the same zero to smaller angle: the nucleus looks larger relative to the probe wavelength. A Woods–Saxon surface replaces the sharp zero by a shallow minimum and fills in $|F|^2$ between lobes, which is why real data never look like an ideal sphere.

Remark

Limits. The Born/PWBA reading $F(q) = \tilde{\rho}_{\mathrm{ch}}(q)/\tilde{\rho}_{\mathrm{ch}}(0)$ assumes a weak Coulomb distortion. For heavy targets and low E, distorted-wave analyses shift extracted radii by a few percent. Charge radii from electron scattering therefore quote the analysis framework, not only a single number R_{eq}.

Key idea

Physical meaning. Form-factor zeros encode a length. Skin thickness t damps high-q oscillations. Lecture 2's saturation density is the bulk plateau behind that surface; Lecture 3's isotope shifts track changes in $\langle r^2\rangle$ along a chain without remeasuring the whole $F(q)$.

1.11.2 Reading diffraction like optics

Optical Babinet intuition helps: a circular aperture of radius R has Airy zeros set by qR, while a soft edge (the nuclear surface) suppresses higher rings. Empirically, the equivalent uniform radius extracted from the first minimum and the rms radius from the small-q slope differ by ~ 0.2–$0.5\,\mathrm{fm}$ in heavy nuclei. Quoting only one without stating the definition confuses comparisons across experiments.

A second practical point is beam energy. At $E \sim 50\,\mathrm{MeV}$ the accessible q barely samples the surface; at several hundred mega-electronvolts one resolves interior oscillations of ρ_{ch}. Hofstadter's programme succeeded because both the Mott baseline and a wide q lever arm were available. Students reconstructing $F(q)$ from a published ρ_{ch} should always overlay the Mott-reduced cross section, not only the form factor, so that normalisation systematics remain visible.

The Coulomb sum rule and longitudinal/transverse separations in quasi-elastic scattering extend the same electron probe beyond elastic form factors, but they lie outside this chapter's elastic focus. Keep the elastic lesson sharp: $F(q)$ is the Fourier transform of charge, zeros encode size, and surface thickness encodes diffuseness.

The multipole expansion of the charge density also clarifies magnetic versus charge scattering:

elastic magnetic form factors (odd-mass targets) probe magnetisation densities and thereby connect to Schmidt moments in Lecture 14, while this chapter restricts attention to charge form factors of even-even systems whenever possible. Keeping charge and magnetisation channels separate prevents mis-reading a magnetic minimum as a charge radius. For classroom estimates, computing both the uniform-sphere zero and the Gaussian form factor $F = \exp(-q^2\langle r^2\rangle/6)$ at the same $\langle r^2\rangle$ shows how surface diffuseness alone moves strength from the diffraction minimum into the fills between lobes.

1.12 Further physics: light nuclei, rms radii, and halos

Electron scattering does not give a single number "the radius." Heavy nuclei have nearly flat central charge densities that fall over a skin of thickness ~ 2.3 fm. Light nuclei ($A \lesssim 20$) often have densities peaked near $r = 0$, so a hard-sphere radius is less useful than the rms radius

$$\langle r^2\rangle = \frac{\int r^2 \rho(r)\, \mathrm{d}^3 r}{\int \rho(r)\, \mathrm{d}^3 r}, \qquad r_{\mathrm{rms}} = \sqrt{\langle r^2\rangle}. \tag{1.46}$$

For a uniform sphere of radius R, $r_{\mathrm{rms}} = \sqrt{3/5}\, R$. Typical values from electron scattering are $r_{\mathrm{rms}}(^{12}\mathrm{C}) \approx 2.4$ fm, $r_{\mathrm{rms}}(^{16}\mathrm{O}) \approx 2.7$ fm, $r_{\mathrm{rms}}(^{208}\mathrm{Pb}) \approx 5.5$ fm, while the deuteron is anomalously large, $r_{\mathrm{rms}}(^{2}\mathrm{H}) \approx 2.1$ fm for only two nucleons [14, 6].

Some loosely bound systems form **halo nuclei**: one or two valence nucleons orbit a compact core at large distance. An example is ^{11}Be (one neutron outside ^{10}Be), where the valence neutron rms radius can reach ~ 6 fm while the core is only ~ 2.5 fm. Such extremes underline that $R = r_0 A^{1/3}$ is a bulk average, not a universal law for every light species [14].

1.12.1 Quantitative rms radii

Selected rms charge radii from electron scattering [14] (approximate values):

Nucleus	r_{rms} (fm)	equiv. $R = \sqrt{5/3}\, r_{\mathrm{rms}}$	$R/A^{1/3}$
^{1}H	0.84–0.88	~ 1.1	—
^{2}H	2.1	2.7	~ 2.2 (anomalous)
^{4}He	1.7	2.1	~ 1.3
^{12}C	2.5	3.2	~ 1.3
^{16}O	2.7	3.5	~ 1.4
^{40}Ca	3.5	4.5	~ 1.3
^{208}Pb	~ 5.5	~ 7.1	~ 1.2

Heavy nuclei approach $R \approx 1.2\, A^{1/3}$ fm. The deuteron is an outlier because its wave function extends far beyond the range of the NN force (Lecture 8).

1.12.2 Skin thickness and constant central density

Electron-scattering charge densities for medium and heavy nuclei share two features [6, 1]:

1. the central density $\rho(0)$ is nearly independent of A (saturation of density);

2. the surface is diffuse: the **skin thickness** t, defined as the distance over which ρ falls from 90% to 10% of its central value, is roughly

$$t \approx 2.3\,\text{fm},$$

almost independent of A.

A hard sphere would have $t = 0$. The finite t is the real-space counterpart of the gradual fall of the form factor $|F(q)|^2$ with momentum transfer. For a sharp sphere of radius R, the form factor involves spherical Bessel functions and has zeros at definite qR; a diffuse surface washes those minima out partially, but the diffraction pattern still fixes R [6, 7].

A fit of rms radii versus $A^{1/3}$ over the chart of the nuclides yields

$$R \approx R_0 A^{1/3}, \qquad R_0 \approx 1.2\text{–}1.25\,\text{fm} \tag{1.47}$$

($R_0 \approx 1.23\,\text{fm}$ is a common electron-scattering value) [6].

1.12.3 Borromean nuclei

A **Borromean** three-body system is bound, while every two-body subsystem is unbound. ^{6}He ($^4\text{He}+n+n$) is the classic nuclear example: the two valence neutrons bind only in the presence of the α core. Halo and Borromean systems show that weak binding and extended wave functions are generic near the drip lines [14].

1.13 Deeper reading: moments of ρ_{ch} from $F(q)$

Expanding $F(q)$ for small q connects diffraction language to rms radii used in atomic and muonic work (Lecture 3):

$$F(q) = 1 - \frac{q^2}{6}\langle r^2\rangle + \frac{q^4}{120}\langle r^4\rangle + \cdots . \tag{1.48}$$

A precision low-q measurement therefore determines $\langle r^2\rangle^{1/2}$ even when the first diffraction minimum is inaccessible. Conversely, mapping several minima constrains higher moments and the surface diffuseness.

1.13.1 Order-of-magnitude check

For lead, $\langle r^2\rangle^{1/2} \simeq 5.5\,\text{fm}$. At $q = 0.5\,\text{fm}^{-1}$ the quadratic term is $q^2\langle r^2\rangle/6 \simeq 0.25$, so $F \simeq 0.75$: already a large finite-size correction, long before the first zero. That is why even modest-q elastic data are nuclear-structure measurements, not mere Rutherford checks.

The same Fourier logic fails for neutrons: the photon couples to charge. Parity-violating scattering (previewed in the research frontier below) isolates the weak charge and thereby the neutron skin, linking Lecture 1's laboratory form factors to the symmetry energy that Lectures 2 and 6 carry into dense matter. When comparing two analyses, ask whether they report charge radius, diffraction radius, or equivalent uniform radius: those three numbers differ once the surface is nonzero.

1.13.2 From elastic form factors to skins

Because neutrons carry almost no charge, elastic $F(q)$ alone cannot fix R_n. Model-dependent hadronic probes and parity-violating asymmetries close that gap. A student exercise that combines a tabulated charge radius with an assumed skin $\Delta R = R_n - R_p$ and then recomputes the weak form factor at the PREX q illustrates how Lecture 1 data enter symmetry-energy fits used in Lectures 2 and 6.

Finally, always propagate the experimental q-calibration and radiative corrections when comparing two $F(q)$ data sets: apparent radius shifts of 0.05 fm are sometimes analysis artefacts rather than new structure.

The multipole expansion of the charge density also clarifies magnetic versus charge scattering: elastic magnetic form factors (odd-mass targets) probe magnetisation densities and thereby connect to Schmidt moments in Lecture 14, while this chapter restricts attention to charge form factors of even-even systems whenever possible. Keeping charge and magnetisation channels separate prevents mis-reading a magnetic minimum as a charge radius. For classroom estimates, computing both the uniform-sphere zero and the Gaussian form factor $F = \exp(-q^2\langle r^2\rangle/6)$ at the same $\langle r^2\rangle$ shows how surface diffuseness alone moves strength from the diffraction minimum into the fills between lobes.

Classroom reconstruction checklist

(1) Digitise or tabulate a published $\rho_{\mathrm{ch}}(r)$. (2) Compute $F(q)$ by numerical Fourier–Bessel transform. (3) Overlay Mott-reduced data if available. (4) Extract $\langle r^2\rangle$ from the small-q slope and compare with the first-minimum radius. (5) Vary the surface diffuseness at fixed rms radius and watch the higher diffraction lobes move. That five-step loop turns Lecture 1 from a plot into a reproducible analysis habit and prepares the isotope-shift discussion of Lecture 3, where only the lowest moments survive.

Error budgets in elastic analyses

Radiative corrections, beam-energy calibration, and target-thickness unfolding each shift apparent diffraction minima. A conscientious comparison of two $F(q)$ data sets therefore begins with the analysis notes, not only with overlaid points. When a modern phase-shift or optical-model Coulomb correction is applied, quote the framework beside any extracted R_{eq}.

Connection to weak probes

The weak charge density weights neutrons more heavily than protons. A parity-violating asymmetry at fixed q is therefore sensitive to R_n once the charge density is known from Lecture 1. Students can treat the charge form factor as an input and vary a two-parameter neutron density until the weak form factor matches a published asymmetry: that toy exercise shows why skins constrain the symmetry energy without yet solving the full many-body problem of Lectures 2 and 6.

Research frontier: neutron skins and future student projects

The elastic electron-scattering form factors of Lecture 1 remain the laboratory standard for nuclear charge densities: Fourier transforms of $\rho_{\mathrm{ch}}(r)$ map diffraction minima to a length scale set by R_{eq}. That programme does not, however, determine the neutron distribution with comparable model independence, because the photon couples to charge. Modern parity-violating electron scattering isolates the weak charge, which is carried mainly by neutrons. The PREX-II measurement on ^{208}Pb reported a neutron skin $R_n - R_p = 0.283 \pm 0.071\,\mathrm{fm}$ and thereby constrained the density dependence of the nuclear symmetry energy near saturation [38, 39]. Ab initio calculations that start from chiral nuclear forces typically predict a thinner skin and remain in tension with that extraction, so the laboratory-theory comparison is an active research question rather than a closed case [40]. What remains uncertain is how much of the discrepancy is experimental systematics, how much is missing many-body correlations, and how much is the mapping from a skin to the slope parameter L. Community roadmaps emphasise completing related experiments (CREX on ^{48}Ca, and future heavy-ion and electron facilities) because the same L that controls the Pb skin also enters crust thicknesses and tidal deformabilities of neutron stars [52].

Beyond the headline skin thickness, a student-ready research question is how to propagate the PREX covariance into a posterior on L without assuming a single Skyrme or relativistic-mean-field family. Comparing several EOS parametrisations side by side, with the same laboratory likelihood, is a concrete way to see model dependence rather than quoting one preferred central value.

Student directions. (1) Analytic estimate: recompute the plane-wave Born form-factor zero for a uniform sphere and compare with Woods–Saxon numerical form factors for $A = 12, 16, 208$. (2) Data project: using tabulated charge radii and the PREX skin, estimate R_n and compare with neutron-star crust-thickness scalings from Lecture 6. (3) Literature note: contrast PREX with CREX and state which observable each experiment constrains, citing the journal results rather than secondary blogs.

1.14 Problems with solutions

The numericals below follow the spirit of Petrera's problem book [3] and standard exercises on nuclear size [6, 1].

Problem 1.1 — Nuclear density (after Petrera 1.1.1)

Estimate the nuclear mass density in $\mathrm{g\,cm^{-3}}$, taking $R = r_0 A^{1/3}$ with $r_0 = 1.2\,\mathrm{fm}$ and neglecting binding energy ($m_p \approx m_n \approx 1.67 \times 10^{-24}\,\mathrm{g}$).

Solution 1.1

Volume $V = \frac{4}{3}\pi R^3$ with $R = r_0 A^{1/3}$ implies

$$\rho = \frac{A\, m_p}{\frac{4}{3}\pi (r_0 A^{1/3})^3} = \frac{3m_p}{4\pi r_0^3}.$$

Insert $m_p = 1.67 \times 10^{-24}$ g and $r_0 = 1.2 \times 10^{-13}$ cm:

$$\begin{aligned} r_0^3 &= (1.2)^3 \times 10^{-39} = 1.728 \times 10^{-39}\,\mathrm{cm}^3, \\ 4\pi r_0^3 &\approx 2.17 \times 10^{-38}\,\mathrm{cm}^3, \\ \rho &= \frac{3 \times 1.67 \times 10^{-24}}{2.17 \times 10^{-38}} \approx 2.3 \times 10^{14}\,\mathrm{g\,cm^{-3}}. \end{aligned}$$

Nuclear matter is about 10^{14} times denser than water. The result is independent of A once saturation and $R \propto A^{1/3}$ are assumed.

Problem 1.2 — Radius from the form factor (after Petrera 1.2.8)

At low momentum transfer the charge form factor admits

$$F(q^2) = 1 - \frac{q^2 \langle r^2 \rangle}{6\hbar^2} + \cdots .$$

Elastic electron scattering at 5° with $p = 720\,\mathrm{MeV}/c$ on $^{12}\mathrm{C}$ gives $\mathrm{d}\sigma/\mathrm{d}\Omega = 80\,\mathrm{mb/sr}$, while the Mott (point) cross section is about $99\,\mathrm{mb/sr}$. Estimate the rms charge radius of carbon.

Solution 1.2

The form factor is the ratio of measured to Mott cross sections:

$$|F|^2 = \frac{80}{99} \approx 0.808 \quad \Rightarrow \quad F \approx \sqrt{0.808} \approx 0.899$$

(positive at small q). Elastic kinematics give

$$q = 2p\sin(\theta/2) = 2 \times 720 \sin(2.5^\circ) = 1440 \times 0.0436 \approx 62.8\,\mathrm{MeV}/c.$$

From $F = 1 - q^2\langle r^2 \rangle / [6(\hbar c)^2] + \cdots$,

$$\begin{aligned} \langle r^2 \rangle &= \frac{6(\hbar c)^2}{(qc)^2}(1 - F) = \frac{6 \times (197\,\mathrm{MeV\,fm})^2}{(62.8\,\mathrm{MeV})^2}(0.101) \\ &\approx \frac{6 \times 38809}{3944} \times 0.101 \approx 59.0 \times 0.101 \approx 5.95\,\mathrm{fm}^2, \end{aligned}$$

so

$$\sqrt{\langle r^2 \rangle} \approx 2.44\,\mathrm{fm}.$$

For a uniform sphere, $R = \sqrt{5/3}\,\sqrt{\langle r^2 \rangle} \approx 3.15\,\mathrm{fm}$, consistent with $r_0 A^{1/3}$ at $A = 12$.

Problem 1.3 — Diffraction estimate of radius

Electrons of energy $E = 180\,\mathrm{MeV}$ scatter elastically from $^{197}\mathrm{Au}$. Treating the nucleus as a hard sphere of radius $R = (1.18A^{1/3} - 0.48)\,\mathrm{fm}$, how many diffraction minima are kinematically accessible (after Petrera 1.2.2)?

Solution 1.3

Uniform-sphere form-factor zeros solve $\tan x = x$ with $x = qR/\hbar$, near $x \approx 3\pi/2,\ 5\pi/2,\ 7\pi/2, \ldots$. Maximum $q \approx 2E/c$, so

$$x_{\mathrm{max}} = \frac{2E}{\hbar c}\,R \approx \frac{2 \times 180}{197} \times 6.4 \approx 11.7.$$

There are three zeros below x_{max} (up to $\sim 7\pi/2$). The angular distribution should show three clear minima.

Bibliography

[1] R. A. Dunlap, *An Introduction to the Physics of Nuclei and Particles* (2nd ed.), IOP Publishing, Bristol (2023), DOI: 10.1088/978-0-7503-6094-4, Ch. 3 (Nuclear composition and size).

[2] W. Demtröder, *Nuclear and Particle Physics*, Undergraduate Lecture Notes in Physics, Springer, Cham (2023).

[3] S. Petrera, *Problems and Solutions in Nuclear and Particle Physics*, UNITEXT for Physics, Springer, Cham (2019).

[4] F. Terranova, *A Modern Primer in Particle and Nuclear Physics*, Oxford University Press (2021).

[5] S. D'Auria, *Introduction to Nuclear and Particle Physics*, Undergraduate Lecture Notes in Physics, Springer, Cham (2018).

[6] K. S. Krane, *Introductory Nuclear Physics*, Wiley, New York (1988).

[7] R. Hofstadter, "Electron scattering and nuclear structure," Rev. Mod. Phys. **28**, 214 (1956).

[8] H. F. Ehrenberg, R. Hofstadter, U. Meyer-Berkhout, D. G. Ravenhall, and S. E. Sobottka, "High-Energy Electron Scattering and the Charge Distribution of Carbon-12 and Oxygen-16," Phys. Rev. **113**, 666 (1959).

[9] H. Yukawa, "On the interaction of elementary particles. I," Proc. Phys.-Math. Soc. Japan **17**, 48 (1935).

[10] R. D. Woods and D. S. Saxon, "Diffuse surface optical model for nucleon-nuclei scattering," Phys. Rev. **95**, 577 (1954).

[11] H. G. J. Moseley, "The high-frequency spectra of the elements," Phil. Mag. **26**, 1024 (1913); **27**, 703 (1914).

[12] C. F. von Weizsäcker, "Zur Theorie der Kernmassen," Z. Phys. **96**, 431 (1935).

[13] P. Cappellaro, *Introduction to Applied Nuclear Physics* (MIT OpenCourseWare / LibreTexts), CC BY-NC-SA 4.0.

[14] J.-L. Basdevant, J. Rich, and M. Spiro, *Fundamentals in Nuclear Physics: From Nuclear Structure to Cosmology*, Springer, New York (2005).

[15] D. Tong, *Particle Physics*, Lecture notes (University of Cambridge / CERN school notes).

[16] M. G. Mayer, "On closed shells in nuclei. II," Phys. Rev. **75**, 1969 (1949).

[17] O. Haxel, J. H. D. Jensen, and H. E. Suess, "On the "magic numbers" in nuclear structure," Phys. Rev. **75**, 1766 (1949).

[18] T. Schmidt, "Über die magnetischen Momente der Atomkerne," Z. Phys. **106**, 358 (1937).

[19] L. W. Nordheim, "On spins, moments, and shells in nuclei," Phys. Rev. **78**, 294 (1950).

[20] Evaluated Nuclear Structure Data File (ENSDF), National Nuclear Data Center, Brookhaven National Laboratory, `https://www.nndc.bnl.gov/ensdf/`.

[21] NuDat 3, National Nuclear Data Center, Brookhaven National Laboratory, `https://www.nndc.bnl.gov/nudat3/`.

[22] N. J. Stone, "Table of nuclear magnetic dipole and electric quadrupole moments," At. Data Nucl. Data Tables **90**, 75 (2005); updated compilations at NNDC.

[23] W. N. Cottingham and D. A. Greenwood, *An Introduction to Nuclear Physics* (2nd ed.), Cambridge University Press, Cambridge (2001).

[24] H. Geiger and J. M. Nuttall, "The ranges of the α particles from the radioactive substances," Phil. Mag. **22**, 613 (1911).

[25] G. Gamow, "Zur Quantentheorie des Atomkernes," Z. Phys. **51**, 204 (1928).

[26] R. W. Gurney and E. U. Condon, "Wave mechanics and radioactive disintegration," Nature **122**, 439 (1928); Phys. Rev. **33**, 127 (1929).

[27] M. Wang, W. J. Huang, F. G. Kondev, G. Audi, and S. Naimi, "The AME 2020 atomic mass evaluation (II). Tables, graphs and references," Chin. Phys. C **45**, 030003 (2021).

[28] Laboratoire National Henri Becquerel (LNHB), Recommended decay data, `http://www.lnhb.fr/nuclear-data/nuclear-data-table/`.

[29] L. M. Langer, R. D. Moffat, and H. C. Price, Jr., "Low energy beta-ray spectra: P^{32} and Cu^{64}," Phys. Rev. **76**, 1725 (1949).

[30] L. M. Langer and H. C. Price, Jr., "Shapes of the beta-spectra of the forbidden transitions of Sb^{124}, Rb^{86}, Sr^{89}, Y^{91}, and Cs^{137}," Phys. Rev. **75**, 1769 (1949).

[31] D. C. Camp and L. M. Langer, "The shape of the ^{66}Ga positron spectrum and the contribution from $0^+ \to 0^+$ transitions," Phys. Rev. **129**, 1782 (1963).

[32] H. C. Verma, *Nuclear Physics: Fundamentals and Applications*, NPTEL/IIT Kanpur lecture series, `https://hcverma.in/ncl_phy_lectures`.

[33] International Atomic Energy Agency, *LiveChart of Nuclides*, evaluated structure, decay, reaction, and fission-yield data, `https://www-nds.iaea.org/relnsd/vcharthtml/VChartHTML.html`.

[34] T. Kibédi, T. W. Burrows, M. B. Trzhaskovskaya, P. M. Davidson, and C. W. Nestor, Jr., "Evaluation of theoretical conversion coefficients using BrIcc," Nucl. Instrum. Methods Phys. Res. A **589**, 202 (2008), DOI: 10.1016/j.nima.2008.02.051.

[35] D. A. Brown *et al.*, "ENDF/B-VIII.0: The 8th major release of the nuclear reaction data library with CIELO-project cross sections, new standards and thermal scattering data," Nucl. Data Sheets **148**, 1 (2018), DOI: 10.1016/j.nds.2018.02.001.

[36] B. Acharya *et al.*, "Solar fusion III: New data and theory for hydrogen-burning stars," Rev. Mod. Phys. **97**, 035002 (2025), DOI: 10.1103/8lm7-gs18.

[37] S. N. Ghoshal, "An experimental verification of the theory of compound nucleus," Phys. Rev. **80**, 939 (1950), DOI: 10.1103/PhysRev.80.939.

[38] D. Adhikari *et al.* (PREX Collaboration), "Accurate determination of the neutron skin thickness of ^{208}Pb through parity-violation in electron scattering," Phys. Rev. Lett. **126**, 172502 (2021), DOI: 10.1103/PhysRevLett.126.172502.

[39] B. T. Reed, F. J. Fattoyev, C. J. Horowitz, and J. Piekarewicz, "Implications of PREX-II on the equation of state of neutron-rich matter," Phys. Rev. Lett. **126**, 172503 (2021), DOI: 10.1103/PhysRevLett.126.172503.

[40] B. Hu *et al.*, "Ab initio predictions link the neutron skin of ^{208}Pb to nuclear forces," Nature Phys. **18**, 1196 (2022), DOI: 10.1038/s41567-022-01715-8.

[41] E. Epelbaum, H.-W. Hammer, and U.-G. Meißner, "Modern theory of nuclear forces," Rev. Mod. Phys. **81**, 1773 (2009), DOI: 10.1103/RevModPhys.81.1773.

[42] H.-W. Hammer, S. König, and U. van Kolck, "Nuclear effective field theory: Status and perspectives," Rev. Mod. Phys. **92**, 025004 (2020), DOI: 10.1103/RevModPhys.92.025004.

[43] T. Otsuka, A. Gade, O. Sorlin, T. Suzuki, and Y. Utsuno, "Evolution of shell structure in exotic nuclei," Rev. Mod. Phys. **92**, 015002 (2020), DOI: 10.1103/RevModPhys.92.015002.

[44] H. Hergert, S. K. Bogner, T. D. Morris, A. Schwenk, and K. Tsukiyama, "The in-medium similarity renormalization group: A novel ab initio method for nuclei," Phys. Rep. **621**, 165 (2016), DOI: 10.1016/j.physrep.2015.12.007.

[45] J. M. Lattimer and M. Prakash, "The equation of state of hot, dense matter and neutron stars," Phys. Rep. **621**, 127 (2016), DOI: 10.1016/j.physrep.2015.12.005.

[46] J. M. Lattimer, "Neutron stars and the nuclear matter equation of state," Annu. Rev. Nucl. Part. Sci. **71**, 433 (2021), DOI: 10.1146/annurev-nucl-102419-124827.

[47] B. P. Abbott *et al.* (LIGO Scientific Collaboration and Virgo Collaboration), "GW170817: Observation of gravitational waves from a binary neutron star inspiral," Phys. Rev. Lett. **119**, 161101 (2017), DOI: 10.1103/PhysRevLett.119.161101.

[48] M. J. Dolinski, A. W. P. Poon, and W. Rodejohann, "Neutrinoless double-beta decay: Status and prospects," Annu. Rev. Nucl. Part. Sci. **69**, 219 (2019), DOI: 10.1146/annurev-nucl-101918-023407.

[49] M. Agostini, G. Benato, J. A. Detwiler, J. Menéndez, and F. Vissani, "Toward the discovery of matter creation with neutrinoless $\beta\beta$ decay," Rev. Mod. Phys. **95**, 025002 (2023), DOI: 10.1103/RevModPhys.95.025002.

[50] P. Gysbers *et al.*, "Discrepancy between experimental and theoretical β-decay rates resolved from first principles," Nature Phys. **15**, 428 (2019), DOI: 10.1038/s41567-019-0450-7.

[51] H. L. Crawford, K. Fossez, S. König, and A. Spyrou, "A vision for the science of rare isotopes," Annu. Rev. Nucl. Part. Sci. **74**, 141 (2024), DOI: 10.1146/annurev-nucl-121423-091501.

[52] Nuclear Science Advisory Committee, *A New Era of Discovery: The 2023 Long Range Plan for Nuclear Science*, U.S. Department of Energy and National Science Foundation (2023), `https://nuclearsciencefuture.org/`.

[53] S. A. Giuliani, Z. Matheson, W. Nazarewicz, E. Olsen, P.-G. Reinhard, J. Sadhukhan, B. Schuetrumpf, N. Schunck, and P. Schwerdtfeger, "Colloquium: Superheavy elements: Oganesson and beyond," Rev. Mod. Phys. **91**, 011001 (2019), DOI: 10.1103/RevModPhys.91.011001.

[54] N. Schunck and D. Regnier, "Theory of nuclear fission," Prog. Part. Nucl. Phys. **125**, 103963 (2022), DOI: 10.1016/j.ppnp.2022.103963.

[55] I. Counts, J. Hur, D. P. L. Aude Craik, H. Jeon, C. Leung, J. C. Berengut, A. Geddes, A. Kawasaki, W. Jhe, and V. Vuletić, "Evidence for nonlinear isotope shift in Yb^+ search for new boson," Phys. Rev. Lett. **125**, 123002 (2020), DOI: 10.1103/PhysRevLett.125.123002.

[56] I. Angeli and K. P. Marinova, "Table of experimental nuclear ground state charge radii: An update," At. Data Nucl. Data Tables **99**, 69 (2013), DOI: 10.1016/j.adt.2011.12.006.

[57] S. Kraemer *et al.*, "Observation of the radiative decay of the ^{229}Th nuclear clock isomer," Nature **617**, 706 (2023), DOI: 10.1038/s41586-023-05894-z.